Low-Profile and Broadband Dual-Linearly Polarized Offset Dual-Reflector Antenna for W-band Applications

Thi-Kim-Ngan Nguyen, Jérôme Taillieu, David González-Ovejero, Ronan Sauleau

Communication

Low-Profile and Broadband Dual-Linearly Polarized Offset Dual-Reflector Antenna for W-band Applications

Thi-Kim-Ngan Nguyen, Jérôme Taillieu, David González-Ovejero, and Ronan Sauleau

***Abstract*—A low-profile, broadband, dual-linearly polarized offset dual-reflector antenna is presented for high-gain operation at W-band (75-110 GHz). The dual-linear polarization is achieved by exciting two orthogonal modes in an overmoded parallel plate waveguide (PPW), namely the quasi-TEM mode and the quasi-TE$_1$ mode. The offset dual-reflector system is illuminated by a dual-mode corrugated feed horn in the PPW. Since the reflector system only collimates the beam in one plane, an exponentially flared section is integrated at the end of its radiating aperture to collimate the beam in the orthogonal plane. The antenna is built in Aluminum and fabricated as a split block using computer numerical control (CNC) milling. Experimental results show an input reflection coefficient better than −10 dB over a fractional bandwidth exceeding 38% for the two modes of operation. A good agreement is observed between simulated and measured far-field patterns for both operating modes, thus validating the antenna concept. The measured gain remains stable over the entire W-band with a maximum value of 28.8 dBi and 28.5 dBi for the quasi-TEM mode and the quasi-TE$_1$ mode, respectively.**

***Index Terms*—Offset dual-reflector system, parallel plate waveguide (PPW), dual-linear polarization, corrugations, mm-wave antennas.**

I. Introduction

Emerging wireless applications and services demand for high-capacity public and private networks [1]. Mm-wave backhaul and fronthaul solutions have emerged as promising options in this context due to their ease of deployment and potential to provide high data rates with low latency. These solutions can be deployed in various scenarios, including small cells, wireless mesh networks, and point-to-point communication links [2]. The antennas for these systems must be low-profile, highly directive, and exhibit a high radiation efficiency over a large bandwidth to compensate for an increased material dissipation and the significant free space path loss (FSPL) at mm-wave frequencies.

Manuscript received xx, 2024; revised xx, 2024; accepted xx, xxxx. Date of publication xx, xxxx; date of current version xx, xxxx. This work was supported by the European Union through European Regional Development Fund (ERDF), Ministry of Higher Education and Research, CNRS, Brittany region, Conseils Départementaux d'Ille-et-Vilaine and Côtes d'Armor, Rennes Métropole, and Lannion Trégor Communauté, through the CPER Project CyMoCod. (*Corresponding author: David González-Ovejero.*)

T.K.N Nguyen, D. González-Ovejero and R. Sauleau are with Univ Rennes, CNRS, Institut d'Électronique et des Technologies du numéRique (IETR)-UMR 6164, F-35000 Rennes, France (e-mail: thi-kim-ngan.nguyen@univ-rennes.fr; david.gonzalez-ovejero@univ-rennes.fr; ronan.sauleau@univ-rennes.fr).

Jérôme Taillieu is with Univ Rennes, CNRS, Institut d'Électronique et des Technologies du numéRique (IETR)-UMR 6164, F-35000 Rennes, France, and is with Univ Rennes, CNRS, Institut FOTON-UMR 6082, F-35000 Rennes, France (e-mail: jerome.taillieu@univ-rennes.fr).

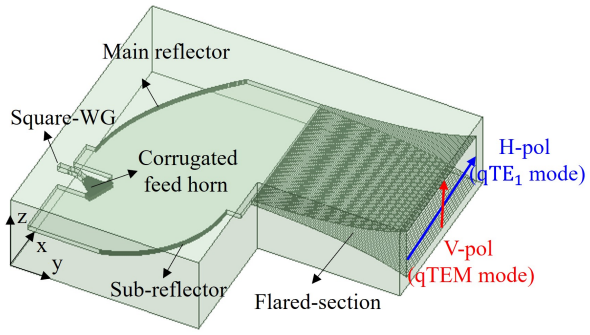

Fig. 1. Perspective view of the dual-linearly polarized offset dual-reflector antenna in the overmoded parallel plate waveguide (OPPW).

One popular solution for achieving low-profile, wide-band, beam scanning, and high-gain mm-wave antennas [3] involves using quasi-optical beamformers integrated in parallel-plate waveguides (PPWs). On the one hand, there are quasi-planar lens-based beamformers for multi-beam antennas, which encompass the classical Rotman lens [4], Luneburg lens [5], [6] and reflecting Luneburg lens [7], [8]. On the other hand, reflector-based beamformers for realizing multi-beam antennas at mm-wave frequencies have been developed either in a single-layer configuration [9]–[11] or in double-layer structures, such as pillbox couplers [12]–[15].

One fundamental shortcoming of the aforementioned quasi-optical beamformers in PPW is that they are inherently limited to a single linear polarization, since their operation primarily relies on the fundamental transverse electromagnetic (TEM) PPW mode. A dual-polarized continuous transverse stubs (CTS) array antenna at Ka-band was introduced in [16], where the conventional PPW was replaced with a corrugated parallel plate waveguide (CPPW). The main advantage of employing CPPW lies in its ability to support two orthogonally-polarized propagating modes, specifically the quasi-TEM and the first order quasi-transverse electric (quasi-TE$_1$) mode, while effectively suppressing the quasi-transverse magnetic (quasi-TM$_1$) and other higher-order modes. Building on the concept of dual-mode excitation in the overmoded PPW (OPPW), a single offset reflector design was presented in [17]. Here, a dual-linearly polarized offset dual-reflector antenna is designed at W-band. The proposed structure presents a low-profile and provides a high gain over a broad frequency band for two orthogonal linear polarizations. To the best our our knowledge, this is the first demonstration of a PPW antenna with integrated reflectors operating in dual-linear polarization.

This communication is organized as follows. Section II

This article has been accepted for publication in IEEE Transactions on Antennas and Propagation. This is the author's version which has not been fully edited and content may change prior to final publication. Citation information: DOI 10.1109/TAP.2024.3458183

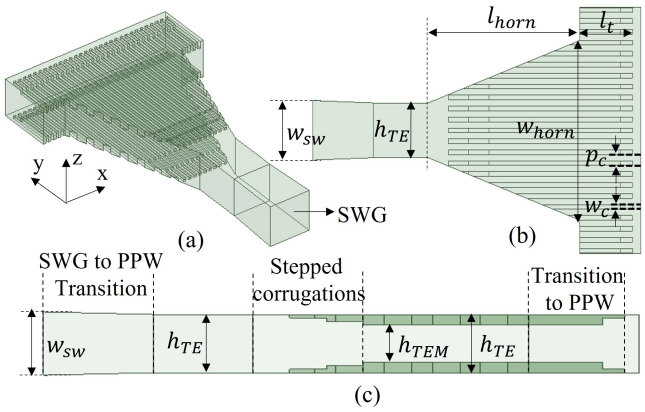

Fig. 2. Drawing and geometrical parameters of the dual-mode corrugated feed horn excited by a square waveguide (SWG). (a) Perspective view. (b) Top-view. (c) Cross-sectional view. Values of the design parameters (in mm): $l_{horn} = 8.3$, $w_{horn} = 8.3$, $l_t = 3.3$, $p_c = 0.376$, $w_c = 0.165$, $h_{TEM} = 1.5$, $h_{TE} = 2.3$, $w_{sw} = 2.54$.

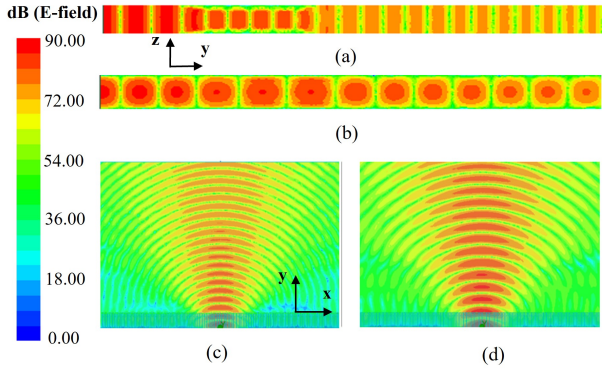

Fig. 3. Amplitude distribution (in dB) of the E-field inside the PPW at 90 GHz for the quasi-TEM mode in the (a) yz-plane and (c) xy-plane; for the quasi-TE$_1$ mode in the (b) yz-plane and (d) xy-plane.

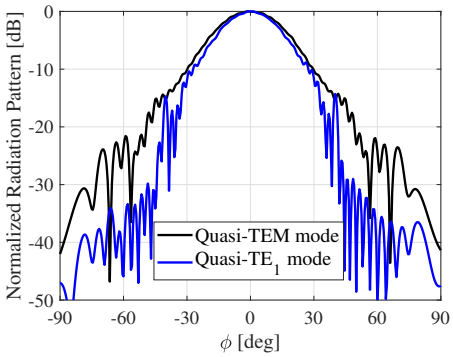

Fig. 4. Normalized radiation patterns computed in the xy-plane of the corrugated feed horn for dual-mode excitation at 90 GHz.

describes the antenna architecture and the design procedure, thoroughly explaining the achievement of dual-linear polarization. Section III presents the fabricated prototype and the experimental results of the overall antenna system, while discussing the impact of fabrication tolerance. Finally, conclusions are drawn in Section IV.

II. Antenna Architecture and Design Procedure

Fig. 1 shows a perspective view of the antenna architecture, which is fully realized in Aluminum and consists of three main parts: a dual-mode corrugated feed horn, an offset dual-reflector in PPW, and a flared transition towards the radiating aperture. The antenna working principles and design procedure are explained in this section, where the simulation results have been obtained using Ansys HFSS version 20.1.

A. Dual-Mode Corrugated Feed Horn

First, we discuss the dual-mode feed horn design in an OPPW with a height ranging from half to one wavelength. In addition to the fundamental TEM mode, this structure supports the higher-order TE$_1$ and TM$_1$ modes. As investigated in [16], there exists a strong mutual coupling between TEM and TM$_1$ modes, especially at any discontinuity in the PPW, owing to their E-fields sharing the same polarization. In contrast, the E-field lines for TEM and TE$_1$ modes are orthogonal, and their mutual coupling is thus negligible. To achieve the propagation of two orthogonally-polarized modes (TEM and TE$_1$) in the OPPW without degrading their radiation characteristics, it is essential to suppress the propagation of the TM$_1$ mode. One effective solution consists of periodically introducing longitudinal corrugations on the waveguide contour, creating a CPPW. These longitudinally corrugated plates perform as electromagnetic hard surfaces [18], which support propagating waves at the surface for any polarization. By modifying the boundary conditions imposed on the parallel plates, the quasi-TM$_1$ is effectively suppressed within a certain frequency range.

Fig. 2 shows the geometry of the corrugated feed horn designed at the center frequency of 90 GHz. The input square waveguide (SWG) can launch both a z-polarized E-field (quasi-TEM mode or vertical polarization) and an x-polarized E-field (quasi-TE$_1$ mode or horizontal polarization) inside the PPW. The two parallel plates are separated by distance h_{TE}, whereas the distance between upper and lower longitudinal corrugations is h_{TEM}. The width of the corrugations and their periodicity are denoted w_c and p_c, respectively, both of which are much smaller than the wavelength λ. To ensure that only the propagation of the quasi-TE$_1$ and quasi-TEM modes occurs in the frequency range between f_{low} and f_{high}, the following conditions are enforced

$$0 < h_{TEM} < \lambda_{high}/2, \tag{1}$$

$$\lambda_{low}/2 < h_{TE} < \lambda_{high}, \tag{2}$$

where λ_{high} and λ_{low} are the free-space wavelength at the higher and lower frequencies, respectively.

From (1), the quasi-TEM mode can propagate within the region of the PPW bounded by the corrugations, defined as $-h_{TEM}/2 < z < h_{TEM}/2$. However, the quasi-TM$_1$ mode is evanescent in this region, as the corrugated surfaces effectively act as uniform metal plates for z-polarized fields, thereby preventing unwanted TEM-TM$_1$ mode coupling. The quasi-TEM field does not propagate in the region confined between the corrugations and continuous metallic plates, as depicted in Fig. 3(a). Fig. 3(b) shows the E-field profile of the quasi-TE$_1$ mode, which is extended to the whole PPW height, i.e. $-h_{TE}/2 < z < h_{TE}/2$.

This article has been accepted for publication in IEEE Transactions on Antennas and Propagation. This is the author's version which has not been fully edited and content may change prior to final publication. Citation information: DOI 10.1109/TAP.2024.3458183

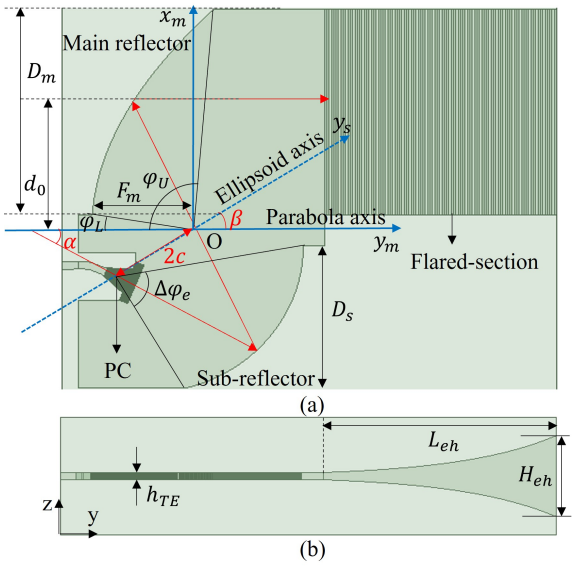

Fig. 5. Geometry of the offset dual-reflector system with an integrated flared section. (a) Top-view. (b) Cross-sectional view. Values of the design parameters: $D_m = 66.6\,\text{mm}$, $F_m = 33.3\,\text{mm}$, $d_0 = 38.3\,\text{mm}$, $D_s = 45.7\,\text{mm}$, $2c = 14.83\,\text{mm}$, $\Delta\varphi_e = 64°$, $\varphi_U = 8.6°$, $\varphi_L = 94.14°$, $\alpha = 37.3°$, $\beta = 30°$, $L_{eh} = 73.26\,\text{mm}$, $H_{eh} = 26.15\,\text{mm}$.

It is important to note that the width and the period of the corrugations are optimized to achieve a similar radiation pattern for both operating modes and to obtain the same illumination taper of the sub-reflector (see Fig. 1), as described in the next section. Figs. 3(c) and (d) show the E-field distributions of the corrugated feed horn in the xy-plane for dual-mode excitation at 90 GHz. Far-field patterns in the xy-plane at 90 GHz are represented in Fig. 4; the quasi-TEM and quasi-TE$_1$ modes exhibit similar radiation patterns, with a half-power beamwidth (HPBW) of $\approx 35°$. These results are obtained when terminating the PPW by a perfectly matched layer (PML).

B. Gregorian Offset Dual-Reflector System with an Exponentially Flared Section

Fig. 5(a) illustrates the geometry and main parameters of the Gregorian offset dual-reflector system. This architecture offers additional flexibility in shaping the plane wavefront amplitude tapering once the feed is fixed. The reflector system is illuminated by the dual-mode corrugated feed horn presented in Section II-A. The main reflector has a parabolic shape and is characterized by its diameter D_m, focal length F_m, and offset distance d_0, in the coordinate system (O, x_m, y_m). The feed horn is oriented at an angle α from the parabola axis y_m. The sub-reflector has an elliptical contour and is described by its diameter D_s, axis tilt angle β, interfocal distance $2c$, and eccentricity e, in the coordinate system (O, x_s, y_s). One focal point of the sub-reflector is positioned at the coordinate system (O, x_m, y_m), while the other one is located at the phase center (PC) of the corrugated feed horn, which is approximately 3.3 mm behind the horn aperture. The profile of the main reflector is given by

$$r_m = \frac{2F_m}{(1 + cos\varphi)}, \tag{3}$$

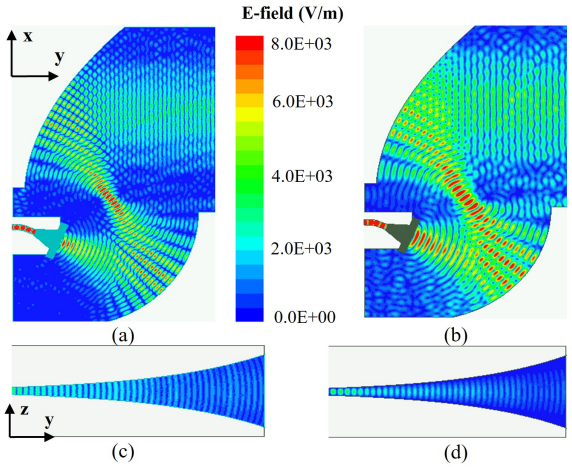

Fig. 6. Amplitude distribution of the E-field in the offset dual-reflector with an integrated flared section at 90 GHz for quasi-TEM mode excitation in (a) the xy-plane and (c) the yz-plane, and for quasi-TE$_1$ mode excitation in (b) the xy-plane and (d) the yz-plane.

where r_m is the distance from the paraboloid focal point to a point on the reflector surface and φ is the angle measured from the main reflector axis to r_m. The sub-reflector profile is a part of the ellipsoid surface and its profile is described as

$$r_s = \left(-\frac{c}{e}\right)\frac{e^2 - 1}{e\cos\beta + 1}, \tag{4}$$

where r_s is the distance between the paraboloid focal point and a point on the sub-reflector surface, β is the angle between the main reflector axis y_m and the sub-reflector axis y_s. The design procedure involves selecting five input parameters including D_m, F_m, d_0, D_s, $\Delta\varphi_e$ and other parameters can be determined by using the equations provided in [19], [20]. The diameter D_m of the main reflector is chosen as a compromise between directivity and antenna size. While increasing the focal length for a given radiation aperture of an offset reflector system can improve cross-polarization levels, it also increases the overall size. As a tradeoff between these factors, the ratio F_m/D_m is set to 0.5. The feed illumination angle $\Delta\varphi_e = 64°$ yields a -11 dB edge tapering for the sub-reflector. The feed pointing angle α is computed using Mizugutch's condition [19] to compensate for the asymmetry of the offset dual-reflector.

The offset dual-reflector system collimates the beam in the xy-plane only. Collimation in the yz-plane is achieved by integrating a flared section after the main reflector. An exponential profile is chosen instead of a linear one to increase the edge illumination taper of the E-field in the yz-plane. The tapering profile is defined by the exponential function

$$f(y) = s_a e^{-y r_a}, \qquad y \in [0; L_{eh}], \tag{5}$$

where $s_a = h_{TE}/2$ and $r_a = 33$.

A cross-sectional view of the flared section and its dimensions are depicted in Fig. 5(b). The height H_{eh} and length L_{eh} of the flared section are chosen as a compromise between the gain and size of the antenna. Figs. 6(a) and (b) illustrate the dual-mode plane wavefront obtained at the reflector aperture by representing the E-field distribution in the xy-plane at 90 GHz. Figs. 6(c) and (d) show the E-field

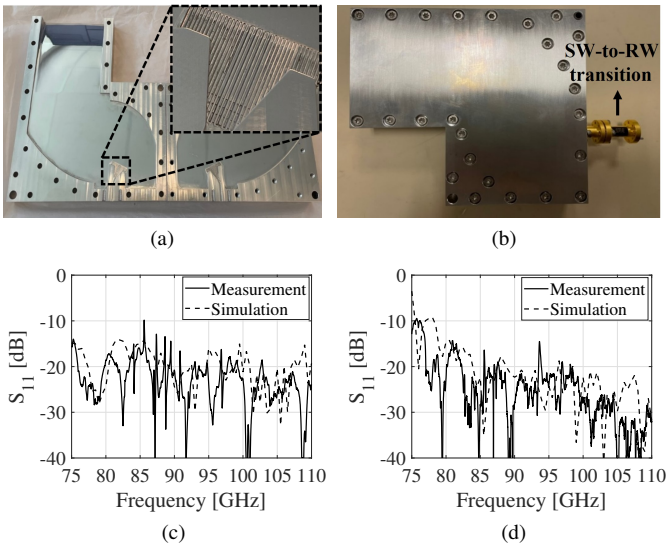

Fig. 7. Pictures of the fabricated prototype: (a) split blocks and (b) assembled prototype. Measured and simulated magnitude (dB) of the input reflection coefficients for (c) the quasi-TEM mode and (d) the quasi-TE_1 mode.

distribution in the yz-plane for the quasi-TEM and quasi-TE_1 modes, respectively. A higher edge illumination level of the E-field is observed in the quasi-TEM mode compared to the quasi-TE_1 mode, which results in higher sidelobe levels in the yz-plane of the quasi-TEM mode.

III. Prototype and Experimental Results

The antenna has been fabricated as a split block using CNC milling, with an accuracy of $10\,\mu$m. Photographs of the fabricated prototype are presented in Fig. 7(a) and (b). The antenna is assembled using screws and dowel pins to ensure electrical contact and alignment between the two aluminum parts. The measurements were conducted using a standard WR10 rectangular waveguide (RW) as input. To that end, two transitions are employed: a WR10-to-circular waveguide (CW) section, and a CW-to-SWG section, as shown in Fig. 7(b). The antenna is excited either by this transition or a $90°$-rotated one to generate orthogonally polarized modes in the input SWG. The entire antenna module, without the waveguide transition, measures $160 \times 148 \times 38\text{mm}^3$, and the size of the radiating aperture is $66.6 \times 26.15\text{mm}^2$ $(20 \times 7.85\lambda_0^2)$. After mechanical assembly, a misalignment of $50\,\mu$m along the x-axis is measured between the two blocks of the prototype. The effects of this assembly misalignment on the antenna performance are shown next.

The simulated and measured input reflection coefficients of the antenna are plotted in Fig. 7(c) and (d) for the quasi-TEM and quasi-TE_1 modes, respectively. The comparison reveals very good agreement between the simulated and measured results. The measured magnitude of the S_{11} is below $-10\,$dB between 75 and 110 GHz, corresponding to a fractional bandwidth of more than 38% for both modes of operation. These results clearly demonstrate the broadband behavior of the proposed antenna system.

The $50\,\mu$m misalignment observed in the assembled prototype along the x-axis does not affect the input reflection coefficient of the antenna, as clearly shown by the measured

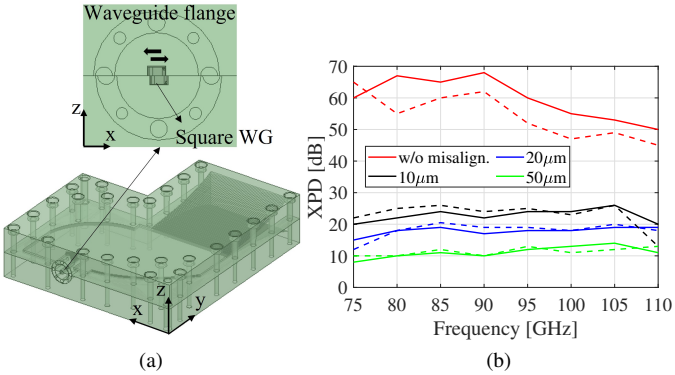

Fig. 8. (a) Misalignment along the x-axis between the two blocks (b) Comparison of simulated cross-polarization discrimination (XPD) in the xy-plane at $\theta = 0°$ for an ideal mechanical assembly and for misalignments of $10\,\mu$m, $20\,\mu$m, and $50\,\mu$m along the x-axis for the quasi-TEM mode (solid lines) and the quasi-TE_1 mode (dash lines).

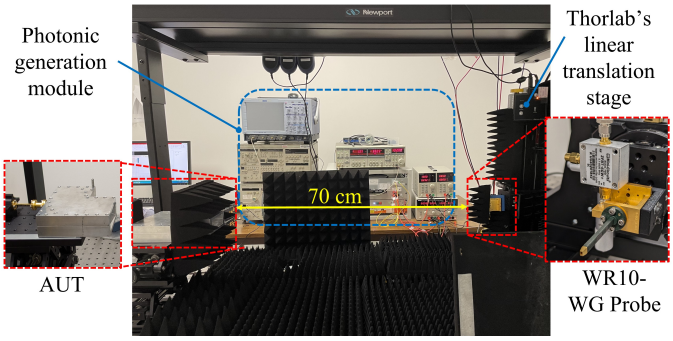

Fig. 9. Antenna radiation pattern far-field measurement setup with a photonic generation system.

S_{11} in Fig. 7(c) and (d). However, it has a significant impact on the cross-polarization levels. Fig. 8 presents an investigation of this effect by evaluating the simulated cross-polarization discrimination (XPD) in the xy-plane at the angle $\theta = 0°$ for several cases of misalignment, including the case of an ideally mechanically assembled antenna. It demonstrates that the XPD levels substantially decrease with greater misalignment along the x-axis for both polarizations. A very similar effect is also observed in the orthogonal plane (yz-plane), but it is not reported here for the sake of brevity. The prototype has been very carefully assembled before performing measurements in radiation to reduce the misalignment error below $20\,\mu$m.

Fig. 9 shows the setup for the radiation pattern measurements along the vertical and horizontal plane cuts. A lock-in reception scheme is used. The mm-wave signal is photonically generated and modulated by a tone from a lock-in amplifier, then coupled to the antenna's input WR10 waveguide. On the receiving side we use a WR10 probe and a zero biased Schottcky detector mounted on the linear motorized translation stage. This stage offers a 30 cm rail range with a 0.5 mm translation step, controlled automatically by the computer. To mitigate undesired reflections or standing waves, the setup is shielded with absorbing panels. Due to the limited length of Thorlab linear stage, the angular coverage in each plane is restricted to between $-15°$ and $15°$. Fig. 10 shows the measured and simulated radiation patterns at four

This article has been accepted for publication in IEEE Transactions on Antennas and Propagation. This is the author's version which has not been fully edited and content may change prior to final publication. Citation information: DOI 10.1109/TAP.2024.3458183

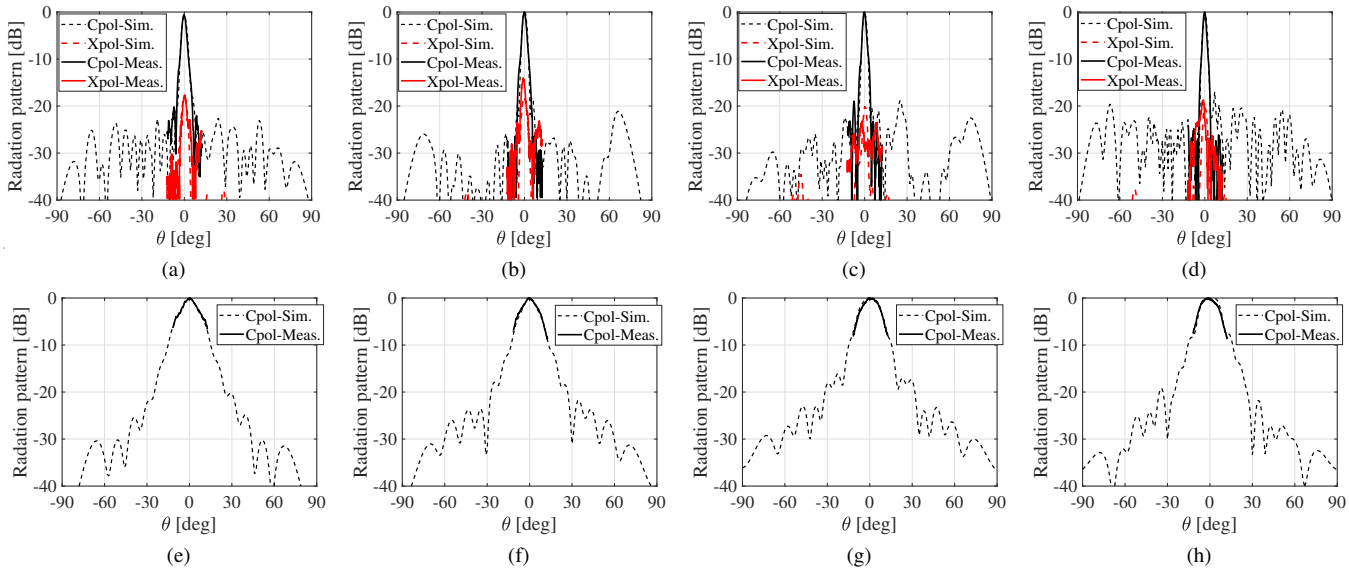

Fig. 10. Normalized radiation patterns for the quasi-TEM mode are shown in the H-plane at (a) 80, (b) 90, (c) 100, and (d) 110 GHz, and in the E-plane at (e) 80, (f) 90, (g) 100, and (h) 110 GHz. Measured co-polarized (solid black lines) and cross-polarized (solid red lines) components are compared with the simulated co-polarized (dotted black lines) and cross-polarized (dotted red lines) components for a 20 μm misalignment.

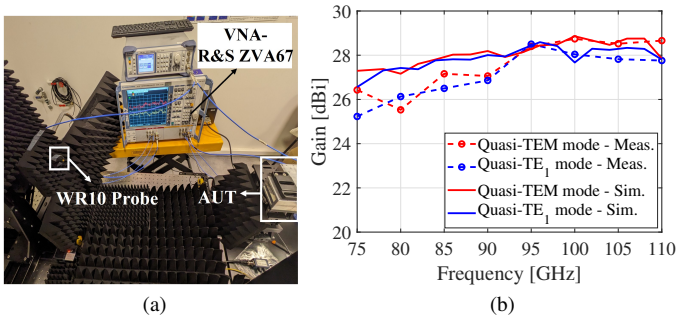

Fig. 11. (a) Antenna gain measurement setup with a VNA. (b) Measured and simulated peak gain of the antenna as a function of frequency.

different frequency points (80, 90, 100, and 110 GHz) in the two principal planes for the quasi-TEM mode, while Fig. 12 does the same for the quasi-TE_1 mode. Good agreements are observed between simulations and measurements in the co-polarized components for both operating modes. In the xy-plane, some of the first measured sidelobe levels (SLLs) can be observed with levels lower than -20 dB and -15 dB over the target frequency band (75–110 GHz) for the quasi-TEM and quasi-TE_1 mode, respectively. The measured cross-polarization level remains < -15 dB below the maximum between 75 and 110 GHz for both operating modes in the xy-plane, which shows a good agreement with the simulated results of the design with 20 μm misalignment. The gain measurement setup is shown in Fig. 11(a), which includes the Vector Netwrok Analyzer VNA-ZVA67, two VNA Extension Modules VNAX959, the antenna under test (AUT) and the receiving WR10 probe. The distance between the AUT and WR10 probe is 796 mm. The measured gain is achieved by comparing the received power with that of a pyramidal reference horn. Fig. 11(b) reports the simulated and measured gain as a function of frequency for both operating modes. The measured gain variation remains below 3 dB over the entire W-band, with the peak gain reaching 28.8 dBi at 100 GHz and 28.5 dBi at 95 GHz under the excitation of the quasi-TEM and quasi-TE_1 modes, respectively. Table I provides a comparison between the presented design and other state-of-the-art PPW antennas with integrated reflector systems at frequencies above 100 GHz, highlighting the competitive performance of the proposed structure, particularly its dual-polarization capabilities.

IV. Conclusion

This work presents a W-band PPW dual-reflector antenna with a unique characteristics, including a low profile, high gain, and a broad bandwidth for dual-linear polarization under the two excitation modes of the OPPW. Measurements of the fabricated prototype confirm the numerical results with an excellent performance: it covers the entire W-band frequency range from 75 to 110 GHz with a gain exceeding 25.6 dBi, and side lobe level lower than -15 dB in the plane collimated by the reflector system, and below -18 dB in the orthogonal plane for both modes of operation. Using alternative assembly procedures or other fabrication technologies (e.g. 3D printing) to mitigate misalignment and air gaps could further enhance the overall antenna efficiency. These results position this antenna as a very attractive candidate for backhaul applications in next-generation telecommunications networks.

References

[1] T. S. Rappaport *et al.*, "Wireless communications and applications above 100 GHz: Opportunities and challenges for 6G and beyond," *IEEE Access*, vol. 7, pp. 78 729–78 757, 2019.

[2] M. Jaber, M. A. Imran, R. Tafazolli, and A. Tukmanov, "5G backhaul challenges and emerging research directions: A survey," *IEEE Access*, vol. 4, pp. 1743–1766, 2016.

[3] Y. J. Guo, M. Ansari, R. W. Ziolkowski, and N. J. G. Fonseca, "Quasi-optical multi-beam antenna technologies for b5G and 6G mmwave and THz networks: A review," *IEEE Open J. Antennas Propag.*, vol. 2, pp. 807–830, 2021.

This article has been accepted for publication in IEEE Transactions on Antennas and Propagation. This is the author's version which has not been fully edited and content may change prior to final publication. Citation information: DOI 10.1109/TAP.2024.3458183

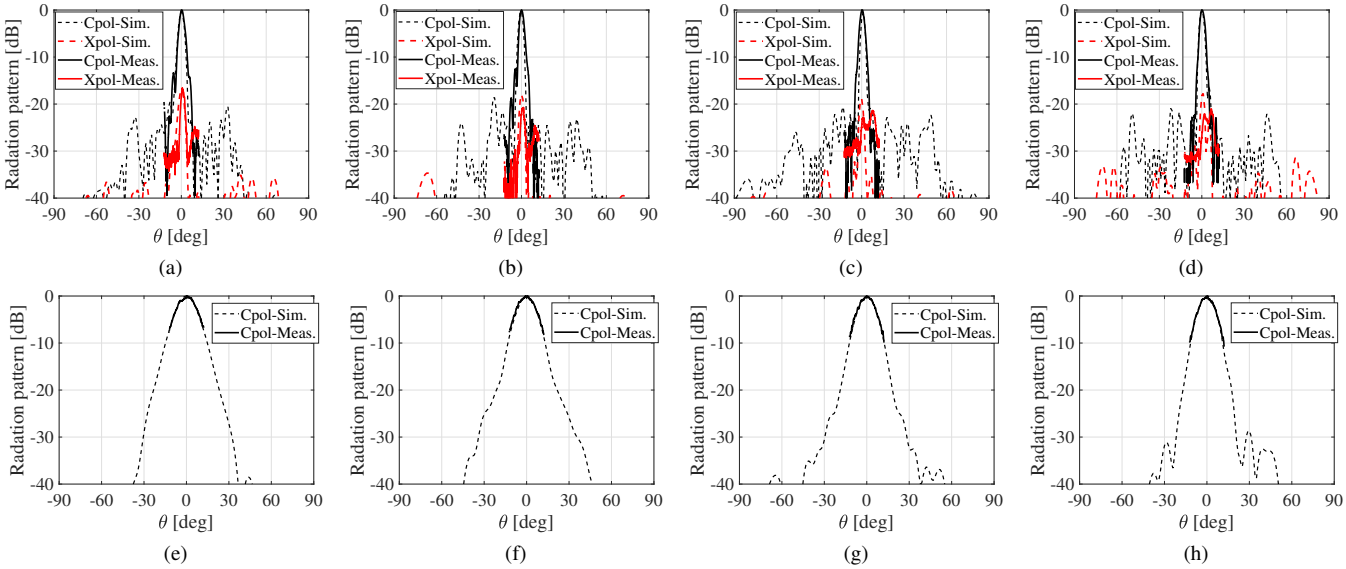

Fig. 12. Normalized radiation patterns for the quasi-TE_1 mode are shown in the E-plane at (a) 80, (b) 90, (c) 100, and (d) 110 GHz, and in the H-plane at (e) 80, (f) 90, (g) 100, and (h) 110 GHz. Measured co-polarized (solid black lines) and cross-polarized (solid red lines) components are compared with the simulated co-polarized (dotted black lines) and cross-polarized (dotted red lines) components for a 20 μm misalignment.

TABLE I
COMPARISON OF STATE-OF-THE-ART PPW ANTENNAS WITH INTEGRATED REFLECTOR SYSTEMS AT FREQUENCIES ABOVE 100 GHZ

Ref.	Architecture	Fabrication technology	Pol.	Profile	BW ($S_{11} < -10$ dB) Freq. range	Max. gain	Aperture Eff.
[14]	LWA fed by pillbox BFN	Micromachining	Single LP	20.8 x 20.8 x 8.8 λ^3	$> 30\%$ 220-330 GHz	28.5 dBi	43%
[11]	Integrated offset dual-reflector	CNC milling	Single LP	64 x 61.3 x 32.6 λ^3	$> 43.75\%$ 325-500 GHz	32 dBi	39%
This work	Integrated offset dual-reflector	CNC milling	Dual LP	48 x 43 x 11.4 λ^3	$> 38.8\%$ 75-110 GHz	qTEM: 28.8 dBi qTE$_1$: 28.5 dBi	30%

[4] N. Jastram and D. S. Filipovic, "Design of a wideband millimeter wave micromachined Rotman lens," *IEEE Trans. Antennas Propag.*, vol. 63, no. 6, pp. 2790–2796, 2015.

[5] D. Pérez-Quintana *et al.*, "Fully metallic Luneburg metalens antenna in gap waveguide technology at V-band," *IEEE Trans. Antennas Propag.*, vol. 71, no. 4, pp. 2930–2937, 2023.

[6] A. Mahmoud, J. Ruiz-García, O. de Sagazan, M. Ettorre, R. Sauleau, and D. González-Ovejero, "Low-cost and low-profile sub-terahertz Luneburg lens beamformer on polymer," *IEEE Antennas Wirel. Propag. Lett.*, vol. 22, no. 6, pp. 1411–1415, 2023.

[7] J. Ruiz-García, E. Martini, C. D. Giovampaola, D. González-Ovejero, and S. Maci, "Reflecting Luneburg lenses," *IEEE Trans. Antennas Propag.*, vol. 69, no. 7, pp. 3924–3935, 2021.

[8] C. Bilitos, X. Morvan, E. Martini, R. Sauleau, S. Maci, and D. González-Ovejero, "Broadband reflecting Luneburg lenses based on bed-of-nails metasurfaces," *IEEE Trans. Antennas Propag.*, vol. 72, no. 2, pp. 1923–1928, 2024.

[9] Y. J. Cheng, W. Hong, and K. Wu, "Millimeter-wave substrate integrated waveguide multibeam antenna based on the parabolic reflector principle," *IEEE Trans. Antennas Propag.*, vol. 56, no. 9, pp. 3055–3058, 2008.

[10] M. Ettorre, A. Neto, G. Gerini, and S. Maci, "Leaky-wave slot array antenna fed by a dual reflector system," *IEEE Trans. Antennas Propag.*, vol. 56, no. 10, pp. 3143–3149, 2008.

[11] K. Fan, Z.-C. Hao, Q. Yuan, and W. Hong, "Development of a high gain 325–500 GHz antenna using quasi-planar reflectors," *IEEE Trans. Antennas Propag.*, vol. 65, no. 7, pp. 3384–3391, 2017.

[12] M. Ettorre, R. Sauleau, and L. Le Coq, "Multi-beam multi-layer leaky-wave SIW pillbox antenna for millimeter-wave applications," *IEEE Trans. Antennas Propag.*, vol. 59, no. 4, pp. 1093–1100, 2011.

[13] E. Gandini, M. Ettorre, M. Casaletti, K. Tekkouk, L. Le Coq, and R. Sauleau, "SIW slotted waveguide array with pillbox transition for mechanical beam scanning," *IEEE Antennas Wirel. Propag. Lett.*, vol. 11, pp. 1572–1575, 2012.

[14] A. Gomez-Torrent *et al.*, "A low-profile and high-gain frequency beam steering subterahertz antenna enabled by silicon micromachining," *IEEE Trans. Antennas Propag.*, vol. 68, no. 2, pp. 672–682, 2020.

[15] T. Potelon, M. Ettorre, and R. Sauleau, "Long slot array fed by a nonuniform corporate feed network in PPW technology," *IEEE Trans. Antennas Propag.*, vol. 67, no. 8, pp. 5436–5445, 2019.

[16] M. Śmierzchalski *et al.*, "A novel dual-polarized continuous transverse stub antenna based on corrugated waveguides—part I: Principle of operation and design," *IEEE Trans. Antennas Propag.*, vol. 69, no. 3, pp. 1302–1312, 2021.

[17] T.-K.-N. Nguyen, D. González-Ovejero, and R. Sauleau, "Low-profile and high-gain dual-linearly polarized offset reflector antenna at W-band," in *Eur. Microw. Conf. (EuMC)*, 2023, pp. 963–966.

[18] P.-S. Kildal, "Artificially soft and hard surfaces in electromagnetics," *IEEE Trans. Antennas Propag.*, vol. 38, no. 10, pp. 1537–1544, 1990.

[19] C. Granet, "Designing classical offset cassegrain or gregorian dual-reflector antennas from combinations of prescribed geometric parameters," *IEEE Antennas Propag. Mag.*, vol. 44, no. 3, pp. 114–123, 2002.

[20] K. Brown and A. Prata, "A design procedure for classical offset dual reflector antennas with circular apertures," *IEEE Trans. Antennas Propag.*, vol. 42, no. 8, pp. 1145–1153, 1994.